L-Band Microwave Emission of Soil Freeze–Thaw Process in the Third Pole Environment

Donghai Zheng, Xin Wang, Rogier van der Velde, Yijian Zeng, Jun Wen, Zuoliang Wang, Mike Schwank, Paolo Ferrazzoli, *Senior Member, IEEE*, and Zhongbo Su

***Abstract*— Soil freeze–thaw transition monitoring is essential for quantifying climate change and hydrologic dynamics over cold regions, for instance, the Third Pole. We investigate the L-band (1.4 GHz) microwave emission characteristics of soil freeze–thaw cycle via analysis of tower-based brightness temperature (T_B^p) measurements in combination with simulations performed by a model of soil microwave emission considering vertical variations of permittivity and temperature. Vegetation effects are modeled using Tor Vergata discrete emission model. The ELBARA-III radiometer is installed in a seasonally frozen Tibetan grassland site to measure diurnal cycles of L-band T_B^p every 30 min, and supporting micrometeorological as well as volumetric soil moisture (θ) and temperature profile measurements are also conducted. Soil freezing/thawing phases are clearly distinguished by using T_B^p measurements at two polarizations, and further analyses show that: 1) the four-phase dielectric mixing model is appropriate for estimating permittivity of frozen soil; 2) the soil effective temperature is well comparable with the temperature at 25 cm depth when soil liquid water is freezing, while it is closer to the one measured at 5 cm when soil ice is thawing; and 3) the impact on T_B^p caused by diurnal changes of ground permittivity is dominating the impact of changing ground temperature. Moreover, the simulations performed with the integrated Tor Vergata emission model and Noah land surface model indicate that the T_B^p signatures of diurnal soil freeze–thaw cycle is more sensitive to the liquid water content of the soil surface layer than the *in situ* measurements taken at 5 cm depth.**

***Index Terms*— L-band microwave radiometry, Noah land surface model (LSM), Soil Moisture and Ocean Salinity (SMOS)/Soil Moisture Active Passive (SMAP), soil freeze/thaw (F/T), Tibetan Plateau, Tor Vergata model.**

Manuscript received December 16, 2016; revised April 2, 2017; accepted May 4, 2017. Date of publication June 5, 2017; date of current version August 25, 2017. This work was supported in part by the Netherlands Organization for Scientific Research under Project ALW-GO/14-29, in part by the National Natural Science Foundation of China under Grant 41405079 and Grant 41530529, and in part by the Key Research Program of the Chinese Academy of Sciences under Grant KZZD-EW-13. *(Corresponding author: Donghai Zheng.)*

D. Zheng, R. van der Velde, Y. Zeng, and Z. Su are with the Faculty of Geo-Information Science and Earth Observation, University of Twente, 7522 NB Enschede, The Netherlands (e-mail: d.zheng@utwente.nl; r.vandervelde@utwente.nl; y.zeng@utwente.nl; z.su@utwente.nl).

X. Wang and Z. Wang are with the Key Laboratory of Land Surface Process and Climate Change in Cold and Arid Regions, Northwest Institute of Eco-Environment and Resources, Chinese Academy of Sciences, Lanzhou 730000, China (e-mail: xinwang@lzb.ac.cn; zuoliangwang@lzb.ac.cn).

J. Wen is with the College of Atmospheric Sciences, Plateau Atmosphere, and Environment Key Laboratory of Sichuan Province, Chengdu University of Information Technology, Chengdu 610225, China (e-mail: jwen@lzb.ac.cn).

M. Schwank is with the Swiss Federal Research Institute WSL, Birmensdorf and Gamma Remote Sensing AG, CH-3073 Gümligen, Switzerland (e-mail: schwank@gamma-rs.ch).

P. Ferrazzoli is with the Dipartimento di Ingegneria Civile e Ingegneria Informatica, Via del Politecnico, University of Rome Tor Vergata, 00133 Rome, Italy (e-mail: paolo.ferrazzoli@uniroma2.it).

Color versions of one or more of the figures in this paper are available online at http://ieeexplore.ieee.org.

Digital Object Identifier 10.1109/TGRS.2017.2705248

I. Introduction

MORE than half of the Northern Hemisphere is covered by permafrost and seasonal frost during winters [1]. The Tibetan Plateau, often referred to as the Third Pole, is also in a substantial part underlain with permafrost and/or subject to seasonally frozen soil [2]. The coexistence of ice and liquid water in frozen soil dramatically alters the soil hydraulic and thermal properties [3] that in turn affects the water and heat distributions across the soil column [4], [5]. In addition, the phase change of soil water, namely, freeze/thaw (F/T) state, at the surface also modulates the surface and subsurface energy partitioning that exerts a profound impact on global and regional climate and hydrology [6]–[8]. It is therefore essential to have accurate information on the soil freeze–thaw state for hydrologic and climate studies over the frozen areas, such as the Third Pole environment.

Information on soil moisture and soil temperature (SMST) and the soil F/T state are generally obtained via *in situ* measurements conducted at the point scale. The SMST and soil F/T state were originally monitored on the plateau along the Qinghai–Tibetan Railway or Highway [9], [10], and several regional-scale SMST monitoring networks [11], [12] have been developed recently for the calibration and validation of soil moisture products derived either from the land surface modeling (LSM) or satellite measurements [13]–[15]. Although these *in situ* measurements have advanced the understanding of soil freeze–thaw process and resulting hydrologic effect of the Tibetan Plateau [16]–[18], their maintenance is time consuming and costly. Furthermore, these point measurements are sparse and less representative of the entire plateau.

On the other hand, previous studies have shown the potential of multifrequency satellite measurements to monitor the soil F/T state from space with active [19]–[21] and passive [22]–[24] microwave sensors. These studies have generally utilized higher frequency measurements (e.g., Ku-, Ka-, and C-band) available from sensors, such as NASA Scatterometer (NSCAT), Special Sensor Microwave Imager (SSM/I), Advanced Microwave Scanning Radiometer-Earth (AMSR-E), and Advanced Scatterometer (ASCAT). Recent studies using Aquarius and Soil Moisture and Ocean Salinity (SMOS) [25] measurements [26]–[28] have demonstrated the feasibility and superiority of L-band (1.4 GHz) passive microwave measurements in monitoring the soil F/T state. Furthermore, NASA's Soil Moisture Active Passive (SMAP) mission launched in January 2015 is a satellite dedicated to estimate soil moisture and to provide information on the soil F/T state using L-band measurements. Microwave measurements at L-band benefit from: 1) relatively high penetration (emission) depth; 2) low effects by overlying vegetation; and 3) weak or even manageable sensitivity to dry snow that results in a better detection of soil F/T state [26], [30], [31].

Ground experiments and theoretical simulations of the microwave signatures of soil freeze–thaw transition have provided the basis for detecting the soil F/T state from the space. Wegmüller [32] measured the brightness temperature (T_B^p, with $p = $ H, V) and backscattering coefficient of diurnal soil freeze–thaw cycle at frequencies between 3 and 11 GHz and developed a semiempirical model to fit the observed behavior that: 1) soil freezing increases the emissivity and decreases the backscattering coefficient and 2) soil thawing leads to the formation of a wet layer at the surface. Zhang *et al*. [33] further showed that the diurnal variation of T_B^p is closely correlated with the phase transition of liquid soil water in frozen soil based on the combined analysis of field experiment and advanced integral equation model (AIEM) model simulations for X-, Ku-, and Ka-band. Experimental investigation and theoretical analysis of L-band microwave radiometry for the soil F/T state detection were presented in [34] and [35] as well, which indicate that the soil freeze–thaw transition has an observable effect on the L-band signature of soil.

This paper further contributes to the understanding of diurnal L-band emission characteristics associated with changing soil F/T state via combined analysis of tower-based ELBARA-III [36] T_B^p measurements and simulations performed with a soil microwave emission model accounting for vertical variations of soil permittivity and soil temperature. Consideration of vegetation effects is made by the Tor Vergata discrete model [37], which was already tested on the Maqu site during warmer seasons [38]. As part of SMOS/SMAP calibration and validation activities, the European Space Agency funded ELBARA-III radiometer is deployed within a well-instrumented regional scale soil moisture and soil temperature (SMST) monitoring network [11] located on the Tibetan Plateau to measure the diurnal cycles of L-band T_B^p every 30 min. Supporting micrometeorological (e.g., solar radiation, air temperature, and humidity) as well as SMST measurements are also conducted.

This paper is outlined as follows. Section II introduces the ELBARA-III field site and *in situ* measurements. Section III describes the emission models and the methods utilized to estimate soil permittivity, effective temperature, and SMST within the surface layer. Section IV provides a description of the analysis on the measured emission characteristics of diurnal soil freeze–thaw transition, and Section V presents the model simulation results. Furthermore, Section VI concludes with a summary of the findings made in this study.

II. Field Site and Measurements

The Maqu regional SMST monitoring network [11], [39] is located in the Source Region of the Yellow River (SRYR) over the northeastern part of the Tibetan Plateau (Fig. 1), which is equipped with about 30 profile measurements of SMST distributed over an area of 40 km × 80 km. The elevation of this area is between 3200 and 4200 m above the sea level. The weather category falls under the class of wet and cold climate according to the updated Köppen–Geiger climate classification. Land cover in this region is dominated by alpine meadows with heights varying from 5 to 15 cm throughout the growing season due to intensive grazing by livestock (e.g., yaks and sheep). The prevailing soil types are sandy loam, silt loam, and organic soil with on average 39.7% sand, 8.1% clay, and a maximum of 18.3% organic matter according to the measurements collected across the SMST network as reported in [39] and [40].

The ELBARA-III radiometer is installed in the center of the SMST monitoring network to obtain radiometric signatures of a seasonally frozen grassland site for the purpose of calibrating and validating SMOS and SMAP brightness temperature (T_B^p). Moreover, continuous measurements of micrometeorological variables and SMST are conducted, and a detailed description of these measurements is provided in the following.

A. ELBARA-III Radiometer

ELBARA-III is an L-band (1.4 GHz) Dicke-type radiometer equipped with a dual-polarized conical horn antenna with -3 dB beamwidth of 12° [36]. It uses a resistive load (RL) and an active cold load (ACL) as internal calibration sources used to derive calibrated T_B^p of ground footprints. The 50-Ω RL is kept at the accurately stabilized instrument internal temperature T_{inst} (better than ±0.1 K) to provide the noise temperature $T_{RL} = T_{inst}$. The ACL is made up of a low-noise amplifier and its noise temperature T_{ACL} is calibrated by means of cold sky measurements. To mitigate and detect potential radio frequency interference (RFI), the received signal is split into two channels, one working between 1.402 and 1.413 GHz and the other between 1.414 and 1.425 GHz, both of which are within the protected part 1.400–1.427 GHz of the microwave L-band (1–2 GHz). The absolute accuracy of ELBARA-III T_B^p measurement is better than 1 K and the corresponding sensitivity is at least 0.1 K according to [36].

At the Maqu site, the ELBARA-III radiometer is mounted on a 4.8-m high tower [Fig. 2(a)], and the center of rotation in elevation (approximately at the same position as the antenna beam waste) is 6.5 m above the ground. The general direction of the antenna beam is toward the south [Fig. 2(d)], and the daily measurements include elevation scanning sequences toward the ground and zenith (sky) measurements. The angular range considered for the elevation scans performed every 30 min is between 40° and 70° (relative to nadir) in steps of 5°. Sky measurements are performed at 23:55 every day with an observation angle of 155°. The horizontal distances d_{min} and d_{max} measured from the radiometer to the closet and the farthest border of the elliptic footprints at -3 dB sensitivity of the antenna are estimated according to [41] and summarized in Table I.

B. Micrometeorology and SMST Profiles

SMST profiles [Fig. 2(b)] are automatically measured next to the radiometer tower [Fig. 2(d)] at 15-min time intervals by 5TM ECH$_2$O probes (Decagon Devices, Inc., USA) installed at the following depths: 5 (×4), 10, 15, 20, 25, 35, 45, 55, 65, 75, 100, and 150 cm. The 5TM probe is a capacitance sensor operating at a 75 MHz measuring the dielectric permittivity of the surrounding soil, and the Topp equation [42] is utilized to convert dielectric permittivity values to volumetric liquid water contents. Furthermore, a specific calibration for the

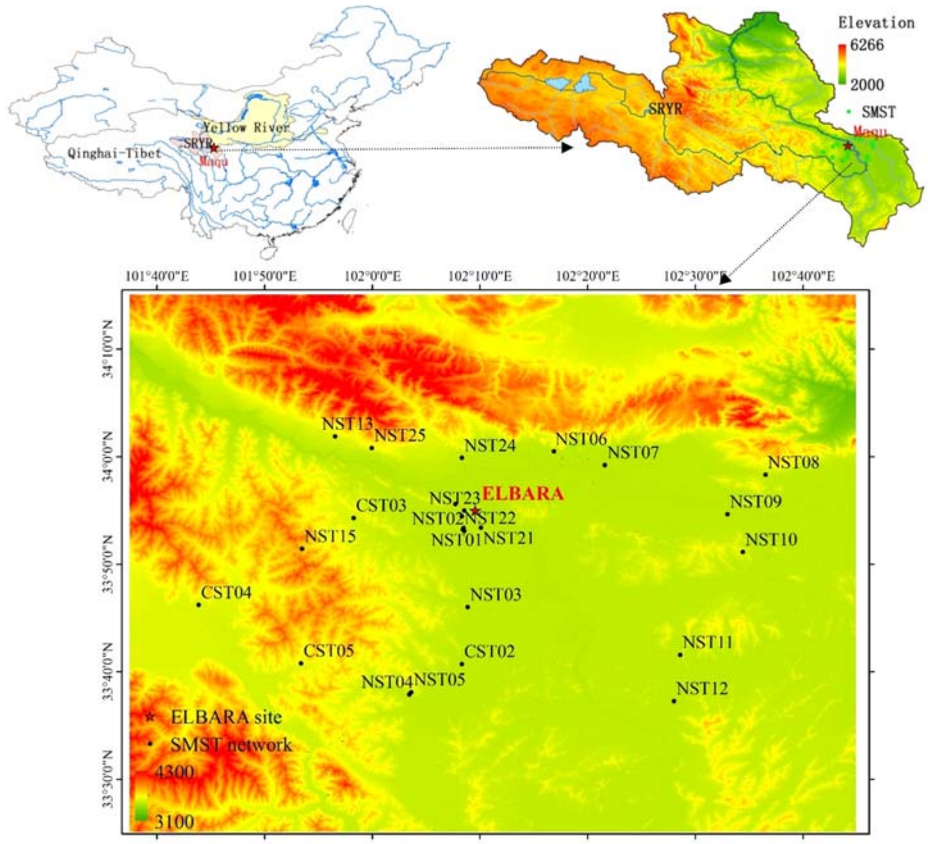

Fig. 1. Location of the SRYR, Maqu SMSTmonitoring network, and the ELBARA-III filed site.

TABLE I
FOOTPRINT DIMENSIONS (AT ≈−3 dB SENSITIVITY) OF ELBARA-III FIELD OF VIEW

Angle (°)	40	45	50	55	60	65	70
$d_{\min}$ (m)	4.38	5.26	6.28	7.48	8.95	10.82	13.33
$d_{\max}$ (m)	6.73	8.03	9.64	11.73	14.6	18.88	26.07

shallow soil layer (i.e., 0–10 cm) with relatively higher organic matter content and deep soil layer (10–160 cm) with relatively lower organic matter content (see Section II-C) is conducted to improve the accuracy of estimated liquid water content as in [39]. This site specific calibration consisted of laboratory measurements of liquid water content of corresponding soil samples taken from the shallow and deep soil layers with both the 5TM probe and the gravimetric method. The soil-specific relation between permittivity and liquid water content consisted of the best fit between these two sets of independent measurements.

The micrometeorological observations [Fig. 2(c)] are performed about 400 m apart from ELBARA-III [Fig. 2(d)]. The observing system consists of a 20-m planetary boundary layer tower providing wind speed and direction, air humidity, and temperature measurements at five heights above the ground, and an eddy-covariance system installed for measuring the turbulent heat fluxes. Instrumentations for measuring four radiation components (i.e., up- and downwelling shortwave and longwave radiations), air pressure, and liquid precipitation are also deployed. The albedo is calculated as the ratio of up- and downwelling shortwave radiations, and the surface temperature is derived from the up- and downwelling longwave radiations as in [43].

C. Soil and Vegetation Parameters

Duplicates of soil samples are collected around the ELBARA-III field site for laboratory analyses to quantify the soil properties affecting soil hydraulics, i.e., soil texture (sand, clay, and silt), organic matter content (m_{soc}), bulk mass density (ρ_b), porosity (θ_s), soil water potential at air entry (ψ_s), and empirical parameters related to the pore-size distribution of the soil matrix (b). Field measurements of the saturated hydraulic conductivity (K_s) are also carried out. The measured hydraulic properties are summarized in Table II, and further details about soil sampling and characterization can be found in [44]. The MODIS leaf area index (LAI) product [MCD15A3H; 45] derived from data acquired by the combined Terra and Aqua satellites is used to represent the vegetation status, and the monthly average values are listed in Table III.

III. MODELS

A. Soil/Vegetation Emission

Simulations were conducted using the model developed at the Tor Vergata University of Rome. This emission model is based on microwave radiative transfer theory and adopts a discrete approach [37]. Both passive [46] and active [47] versions are available. Recently, Dente *et al.* [38] investigated the model performance and demonstrated the model's skill in simulating both emissivity and backscattering coefficient at the Maqu site for nonfrozen soil conditions.

TABLE II
AVERAGED FEATURE OF SOIL PROPERTIES MEASURED BY FIELD AND LABORATORY EXPERIMENTS

Depth (cm)	Sand (%)	Clay (%)	m_{soc} (%)	ρ_b (g cm^{-3})	θ_s (m^3 m^{-3})	ψ_s (m)	b (-)	K_s (10^{-6} m s^{-1})
0-10	49.68	2.19	4.30	1.00	0.563	0.374	6.72	2.30
10-40	46.08	3.75	1.36	1.45	0.454	0.187	7.33	0.94
40-80	68.33	1.15	0.30	1.43	0.415	0.341	3.14	0.68
80-120	73.50	0.96	0.22	1.40	0.455	0.431	3.57	-
120-160	88.40	0.00	0.03	1.42	0.424	0.547	3.17	-

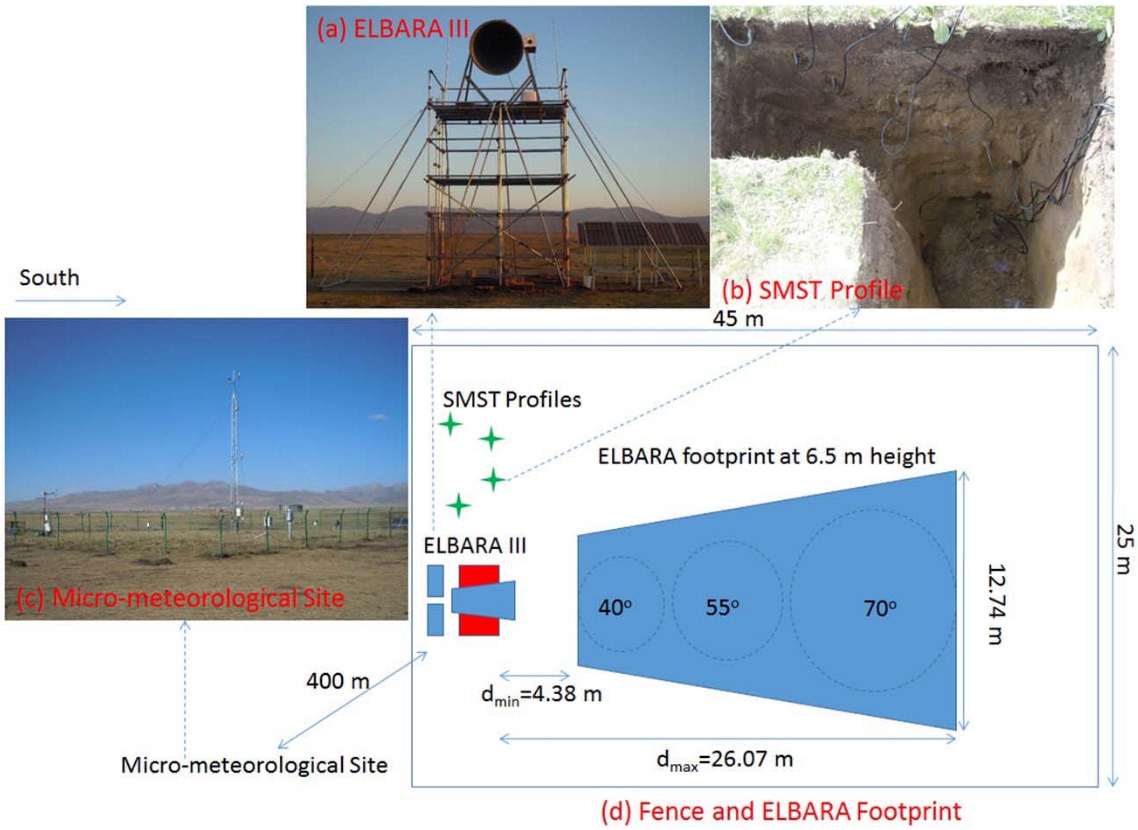

Fig. 2. Fence and footprint of the ELBARA-III field site as well as the deployed measurements.

TABLE III
MONTHLY AVERAGE VALUE OF LAI FOR 2016

Month	January	February	March	April
LAI	0.20	0.23	0.23	0.34

The Tor Vergata model assumes the soil as a homogeneous infinite half space with a rough interface, while the overlying vegetation is represented as an ensemble of discrete dielectric scatterers. As in [38], the grass at the Maqu site is described by thin dielectric disks, and the corresponding electromagnetic properties (i.e., permittivity and bistatic scattering coefficients) are computed by applying the Rayleigh–Gans approximation [48] at L-band. Subsequently, the contributions from individual scatterers (disks) are integrated by adopting the matrix doubling algorithm [48], whereby the overall bistatic scattering and transmissivity are obtained for the whole vegetation canopy. The bistatic scattering coefficient of the soil is represented by the superimposition of a specular coherent component (computed by the Fresnel equations corrected for surface roughness [49]) and a diffuse incoherent component (obtained by the integral equation model (IEM) [50] assuming an exponential autocorrelation function). The specular coherent component is important at L-band [51], especially when the soil permittivity is low (e.g., frozen soil). Furthermore, litter can be included as an extra layer that is treated as a dielectric mixture of air, water, and soil [38], [52]. Finally, the same matrix doubling algorithm is used to combine the vegetation scattering contribution with that of the soil-litter medium.

In the passive version of the Tor Vergata model [46], the overall reflectivity (r^p) of the soil-vegetation system is computed by integrating the bistatic scattering coefficients over the upper hemisphere, and emissivity ($e^p = 1-r^p$) is obtained by applying the energy conservation law. Finally, T_B^p ($=e^p \cdot T_{\mathrm{eff}}$) is computed from the emissivity e^p multiplied by the soil effective temperature T_{eff} (see Section III-B) of the ground. The same physical temperature is attributed to vegetation. This approximation is acceptable, due to the low vegetation emission at L-band, and the sparse areal coverage as is indicated by the very low LAI (see Table III). The contribution of atmospheric emission is calculated based on [53]. In order to estimate the bistatic scattering coefficient of the soil, its permittivity is necessary, which is calculated using the four-phase dielectric mixing model as given in Section III-C.

B. Soil Effective Temperature

The soil effective temperature (T_{eff}) is controlled by the soil dielectric and temperature profiles, which can be expressed as [54]

$$T_{\mathrm{eff}} = \int_0^{\infty} T_s(z)\alpha(z)\exp\left[-\int_0^{z}\alpha(z')dz'\right]dz \qquad (1)$$

where $T_s(z)$ is the soil temperature at depth z and $\alpha(z)$ is the attenuation (absorption) coefficient related to the complex soil dielectric constant $\varepsilon = \varepsilon' + i\cdot\varepsilon''$ at depth z [41]

$$\alpha(z) = \frac{4\pi}{\lambda}\mathrm{Im}(\sqrt{\varepsilon(z)}) \qquad (2)$$

where λ is the wavelength.

The discrete formulation of (1) is given by [55]

$$T_{\mathrm{eff}} = T_{s,1}(1-e^{-\alpha_1\cdot\Delta z_1}) + \sum_{i=2}^{n-1} T_{s,i}(1-e^{-\alpha_i\cdot\Delta z_i})\prod_{j=1}^{i-1} e^{-\alpha_j\cdot\Delta z_j} + T_{s,n}\prod_{k=1}^{n-1} e^{-\alpha_k\cdot\Delta z_k} \qquad (3)$$

where n represents the total number of discrete soil layers, i, j, and k represent the soil layer, T_s is the soil temperature, α is the attenuation coefficient, and Δz is the thickness.

The model for T_{eff} [see (1) and (3)] requires fine-resolution profile information on both soil moisture and temperature, which is, however, usually not available. Therefore, a simple parameterization has been developed for L-band as [54], [56]

$$T_{\mathrm{eff}} = T_{\mathrm{deep}} + (T_{\mathrm{surf}} - T_{\mathrm{deep}})(\theta_{\mathrm{surf}}/\theta_0)^{b_0} \qquad (4)$$

where T_{deep} is the soil temperature at approximately 50 cm depth, T_{surf} is the soil temperature at around 5 cm, θ_{surf} is the soil moisture at around 5 cm, and θ_0 and b_0 are semiempirical parameters mainly depending on the soil texture. For the Maqu site, θ_0 and b_0 are specified as 0.6 m^3 m^{-3} and 0.36, respectively, according to [55]. It should be noted that (4) is mainly applicable for thawed soil, and its validity for frozen soil will be investigated in this study through comparison with the T_{eff} computed by the theoretical formulation.

C. Soil Dielectric Constant and Emission Depth

In frozen soil, the four phases: 1) liquid water; 2) ice; 3) air; and 4) soil matrix coexist, and the resulting effective soil permittivity (ε) is represented using the four-phase dielectric mixing model as [34], [57], [58]

$$\varepsilon^{\eta} = (\theta_s - \theta)\varepsilon_{\mathrm{air}}^{\eta} + \theta_{\mathrm{liq}}\varepsilon_w^{\eta} + (\theta - \theta_{\mathrm{liq}})\varepsilon_{\mathrm{ice}}^{\eta} + (1-\theta_s)\varepsilon_{\mathrm{matrix}}^{\eta} \qquad (5)$$

where θ_s is the porosity, and θ and θ_{liq} represent the total and liquid soil water contents, respectively. The exponent η is set to 0.5, and the dielectric constants of air, ice, and soil matrix are considered as $\varepsilon_{\mathrm{air}} = 1$, $\varepsilon_{\mathrm{ice}} = 3.2 + i\cdot 0.1$, and $\varepsilon_{\mathrm{matrix}} = 5.5 + i\cdot 0.2$ according to [34]. The estimation of the dielectric constant of free (liquid) water (ε_w) at L-band frequency is computed using the model in [49] and [59].

The emission depth (δ_e), defined as the depth over which the electromagnetic power decays by the factor of $e(\approx 2.718)$, is computed as [26], [49]

$$\delta_e = \frac{\lambda}{4\pi}\frac{1}{\mathrm{Im}(\sqrt{\varepsilon(z)})}. \qquad (6)$$

D. Noah Land Surface Model

In the Maqu site, the measurement of top layer soil moisture is generally made at 5 cm depth (Section 2B), and the Noah LSM that has been thoroughly evaluated and augmented for the Maqu area [17], [40], [43], [60] is thus adopted to provide SMST of shallower layers for the calculation of emissivity (see Section V). The Noah model physics associated with freeze–thaw process is briefly outlined subsequently.

The transport of heat through the soil column is governed by the thermal diffusion equation with a source/sink term to account for soil moisture phase transitions [61]

$$C_s(\theta,\theta_{\mathrm{ice}})\frac{\partial T_s}{\partial t} = \frac{\partial}{\partial z}\left(\kappa_h(\theta,\theta_{\mathrm{ice}})\frac{\partial T_s}{\partial z}\right) + \rho_{\mathrm{ice}}L_f\frac{\partial\theta_{\mathrm{ice}}}{\partial t} \qquad (7)$$

where t is the time, ρ_{ice} is the mass density of ice, L_f is the latent heat of fusion, θ_{ice} is the volumetric soil ice content, κ_h is the thermal heat conductivity, and C_s is the thermal heat capacity. Both κ_h and C_s depend on the constituents of the soil matrix (e.g., θ and θ_{ice}), and Zheng *et al.* [60] recently reported that the inclusion of the organic matter effect as is typical for the Tibetan soil, which assumes that each soil layer is a mixture of organic and mineral constituents. The heat source/sink term following from water phase transitions in the soil is determined by assuming the soil water phase equilibrium, which is solved using the water potential-freezing point depression equation in combination with the available heat [61].

The diffusivity form of Richards' equation is utilized to estimate the transport of liquid soil water with the assumption that liquid water flow in frozen soil is analogous to that in unfrozen soil [61]

$$C_s\frac{\partial\theta_{\mathrm{liq}}}{\partial t} = \frac{\partial}{\partial z}\left(D(\theta_{\mathrm{liq}},\theta_{\mathrm{ice}})\frac{\partial\theta_{\mathrm{liq}}}{\partial z}\right) + \frac{\partial K(\theta_{\mathrm{liq}})}{\partial z} + S(\theta) \qquad (8)$$

where D is the soil water diffusivity, K is the hydraulic conductivity, and S represents sources and sinks (i.e., infiltration and evapotranspiration). Detailed descriptions of the D, K, and S parameterizations are given in [17] and [40].

IV. L-Band Emission of Soil Under Freeze/Thaw State

A. Long-Term Analysis

Fig. 3(a) shows time series with a 30-min interval of ELBARA-III measured L-band brightness temperature at both horizontal ($T_{\mathrm{B}}^{\mathrm{H}}$) and vertical ($T_{\mathrm{B}}^{\mathrm{V}}$) polarizations for the period between January 1 (DOY 1) and April 5 (DOY 96), 2016. The data gap is caused by power supply problems. There is not RFI presented during the study period. Only the incidence angles of 40° and 50° are shown due to the fact that the angle 40° is identical to SMAP incidence angle and the T_B^p at 50° is expected to be more sensitive to soil freezing and thawing than other angles [27], [31]. The measured albedo (Section II-B) is also shown to roughly indicate the presence of snowfall and snowpack [62], and the albedo will increase sharply when there is new snowfall and formation of snowpack. It should be noted that the albedo cannot capture well the transition process of existing snowpack between melting and refreezing, and the footprint is much smaller than that of ELBARA-III measurements. As expected, the measured T_B^V values are generally higher than the T_B^H. Two distinct periods can be noted from the T_B^p measurements: 1) a freezing or frozen period from DOY 1 to 76 during which the measured T_B^p remain rather stable and 2) a thawing or thawed period starting from DOY 77 during which the measured T_B^p values are significantly lower and exhibit comparably large temporal variations. Thawing of soil ice increases the effective soil permittivity ε and thus decreases emissivity explaining the observed decrease in T_B^p. The variation of T_B^p at horizontal polarization (T_B^H) is relatively larger than that of T_B^p at vertical polarization (T_B^V) because the effect of changing permittivity is larger for horizontal polarization when considering emission from a Fresnel-like interface [27].

Fig. 3(b) and (c) shows, respectively, the *in situ* measured mean liquid soil water content (θ_{liq}) and soil temperature (T_s) for depths of 5, 25, 55, and 100 cm. The θ_{liq} at 100 cm starts freezing from DOY 26, and the soil above 100 cm is well frozen before DOY 56. Later, the soil ice at 5 cm starts thawing and is totally thawed toward the end of experimental period. Fig. 3(b) also presents the emission depth (δ_e) derived from (6) based on the effective soil permittivity (ε) computed by (5) using θ_{liq} at 5 cm as input, whereby the needed total soil water content (θ) is estimated by linear interpolation between the θ_{liq} measured before and after the freeze–thaw cycle as in [63]. The real part of derived ε ($\varepsilon'_{\text{sim}}$) is further compared with the *in situ* measurements collected by the 5TM probe as shown in Fig. 4(a), and the corresponding error statistics are shown as well, i.e., the coefficient of determination (R^2), mean error, and root-mean-square error (RMSE). Both the low scatter among data points and error statistics indicate that the $\varepsilon'_{\text{sim}}$ values match the measurements fairly well, and a slight underestimation can be noted for higher permittivity values. In general, the derived range $10 \leq \delta_e \leq 30$ cm of emission depth largely depends on the liquid soil water content θ_{liq} taking the lowest value when soil is thawed (maximum θ_{liq}) and taking the highest value for almost frozen soil (minimum θ_{liq}). Furthermore, the theoretical effective temperature ($T_{\text{eff,obs}}$) estimated by (3) using the detailed SMST profile measurements (Section II-B) is also shown in Fig. 3(c). It can be found that the amplitude of the $T_{\text{eff,obs}}$ diurnal cycle is close to the one of T_s at 25 cm due to the contribution of microwave emission from the deeper soil layers [Fig. 3(b)] when the soil is well frozen (before DOY 56) and the θ_{liq} at 5 cm is relatively low, while it is closer to T_s at 5 cm when the soil is thawed in the end of experimental period leading to the shallowest δ_e. The performance of the simple parameterization [see (4)] used to estimate effective soil temperature T_{eff} is also investigated through the comparison between the derived values ($T_{\text{eff,sim}}$) and the $T_{\text{eff,obs}}$ as shown in Fig. 4(b), and the slope of the fitted linear function (equal to unity) and the error statistics confirm its reliability and suitability for frozen soil in the Maqu site.

Fig. 3(d) further shows the measured polarization ratio (PR), i.e., $\text{PR} \equiv (T_B^V - T_B^H)/(T_B^V + T_B^H)$, for the incidence angles of 40° and 50°, and synchronous θ_{liq} at 5 cm is also shown. The two distinct periods found from Fig. 3(a) also become apparent in the shown PR, and a significant increase in PR can be noted around DOY 77 followed by the onset of soil thawing. It implicates that the PR can be treated as a suitable indicator to detect soil thawing in the spring season. Rautiainen *et al.* [26] already reported its potential to detect soil freezing in the autumn season. Further test of soil F/T state detection algorithm such as the one proposed in [26] and [27] needs at least a complete year of T_B^p measurements to appropriately assign the threshold defining F/T state, which is beyond the scope of this study.

B. Diurnal Variations

Two short continuous observation periods, i.e., January 1–6 (DOYs 1–6) and March 28 to April 2 (DOYs 88–93), are selected to further investigate the diurnal characteristics of freezing (or frozen) and thawing (or thawed) soil as shown in the previous section. The diurnal variations of the measured T_B^p, SMST, and albedo for the selected freezing and thawing periods are shown in Figs. 5 and 6, respectively. The real part of the soil permittivity at 5 cm depth measured by the 5TM probe (ε_{obs}) or derived by the four-phase dielectric mixing model (ε_{sim}), as well as the theoretical effective temperature (T_{eff}) computed by (3) is salso shown. During the freezing period, the soil above 65 cm is well frozen [Fig. 5(c)], and θ_{liq} and the permittivity at the surface [Fig. 5(b)] are relatively low. As such, the diurnal variation of T_{eff} is close to the T_s at 25 cm, while its phase remains correlated to the T_s at the surface [Fig. 5(c)]. In contrast, the θ_{liq} and the soil permittivity at the surface [Fig. 6(b)] are comparably higher during the thawing period, and consequently T_{eff} is dominated by surface soil temperature [Fig. 6(c)]. As for the finding of the previous section, the four-phase dielectric mixing model well captures the measurement of permittivity when the soil is frozen, although it is underestimated for thawed soil [Figs. 5(b) and 6(b)]. The four-phase dielectric mixing model [see (5)] for the thawed soil is identical to the one developed in [59] except that a lower value is adopted for the exponent η (0.5 versus 0.65), leading to the underestimation of permittivity. This indicates that different values may be needed for the exponent η depending on the soil F/T state.

In general, the diurnal cycle of the measured T_B^p is the superposition of the diurnal oscillation of the physical soil temperature (i.e., T_{eff}) and the diurnal change of permittivity (i.e., θ_{liq}) within the top soil layer. It can be found that the diurnal magnitude of T_{eff} variation is significantly smaller than that of T_B^p for both freezing and thawing periods [Figs. 5(b) and 6(b)]. Given the sparse vegetation cover (Section II-C), the emissivity e^p of the ground is here derived through normalizing the measured T_B^p by the estimated T_{eff} to further separate the two effects, i.e., $e^p = T_B^p/T_{\text{eff}}$. Obvious diurnal variations are also found for the emissivity e^p associated with freezing and thawing periods

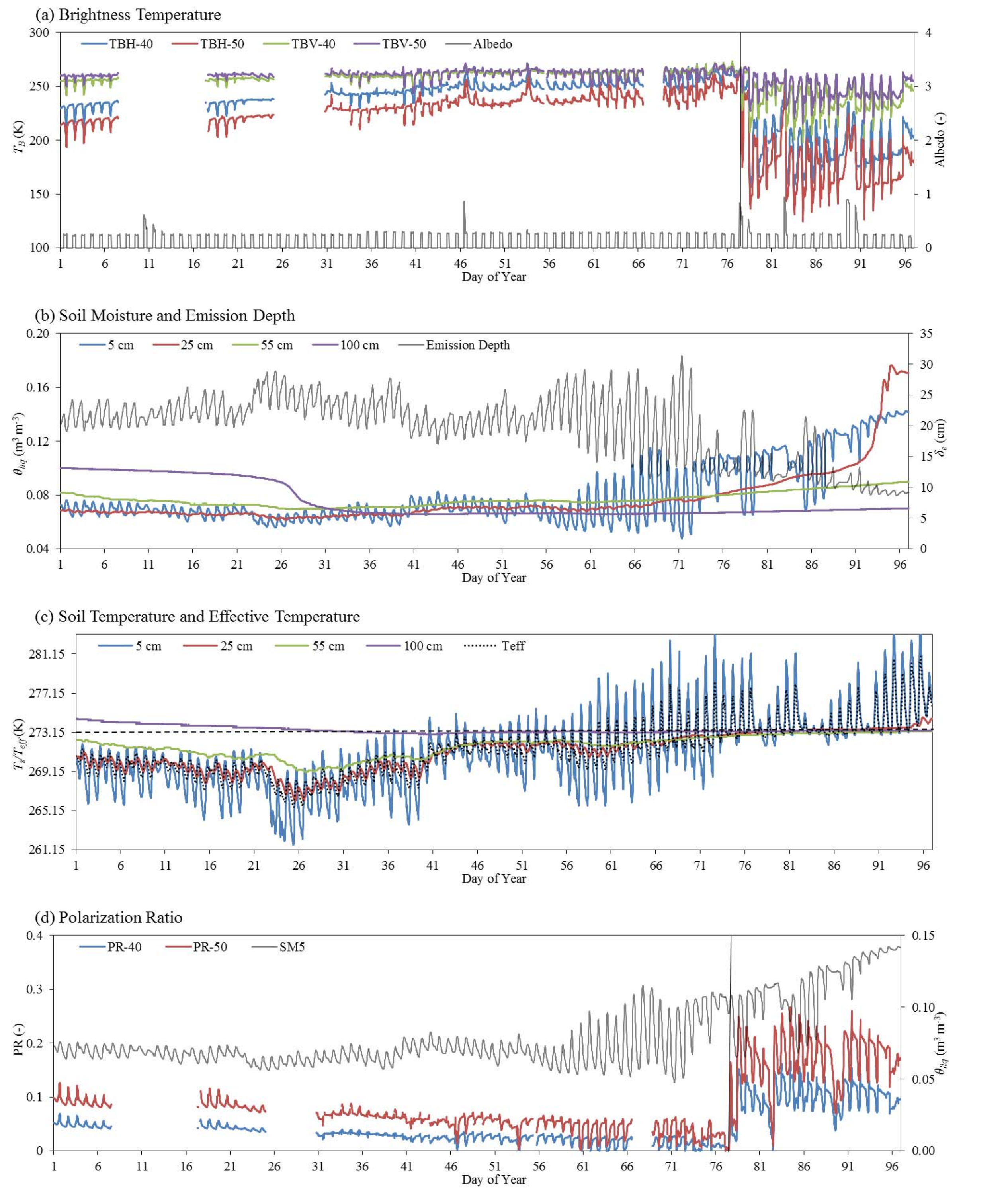

Fig. 3. Measurements with a 30-min interval from January 1 (DOY 1) to April 5 (DOY 96), 2016. (a) Brightness temperature at horizontal ($T_{\mathrm{B}}^{\mathrm{H}}$) and vertical ($T_{\mathrm{B}}^{\mathrm{V}}$) polarizations for incidence angles of 40° and 50° as well as albedo. (b) Liquid soil water (θ_{liq}) at depths of 5, 25, 55, and 100 cm as well as emission depth (δ_e). (c) Soil temperature (T_s) at depths of 5, 25, 55, and 100 cm as well as effective temperature (T_{eff}). (d) PR for incidence angles of 40° and 50°.

[Figs. 5(d) and 6(d)], and the variations of e^p are highly correlated with those of T_{B}^p, which indicates that the changing permittivity associated with the diurnal freeze–thaw transition in the top soil layer corroborates that diurnal variations of T_{B}^p measured are predominantly caused by changes in surface liquid soil water content. Specifically, the water at the surface is freezing between 0 and 11 h followed with decreasing permittivity between DOYs 1–6 (freezing period) due to decrease of T_s (Fig. 5), causing slightly increased e^p. Later, the θ_{liq} and permittivity increase gradually and reach the diurnal peak at around 18 h as a result of soil thawing, leading to the drop down of both e^p and consequently T_{B}^p. The refreezing of θ_{liq} between 19 and 24 h increases again the e^p and T_{B}^p. Similarly, the freezing of θ_{liq} leads to the increase in both e^p and T_{B}^p

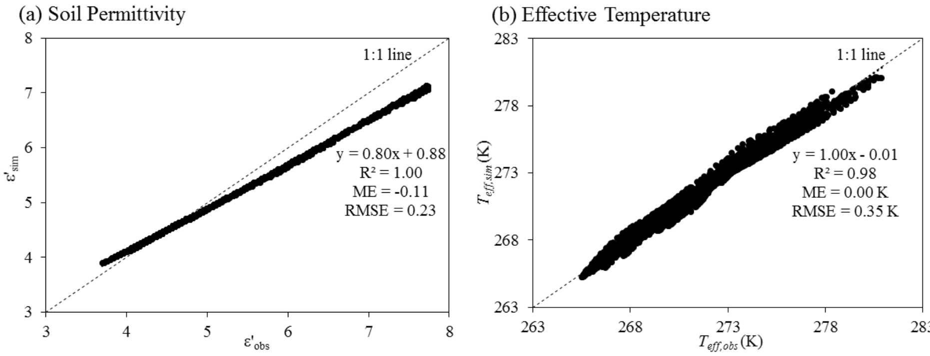

Fig. 4. Scatterplots of (a) real part of effective soil permittivity measured by 5TM probe ($\varepsilon'_{\mathrm{obs}}$) and simulated with four-phase dielectric mixing model ($\varepsilon'_{\mathrm{sim}}$) and (b) effective temperature derived by theoretical formulation [(3), $T_{\mathrm{eff,obs}}$] and a simple parameterization [(4), $T_{\mathrm{eff,sim}}$].

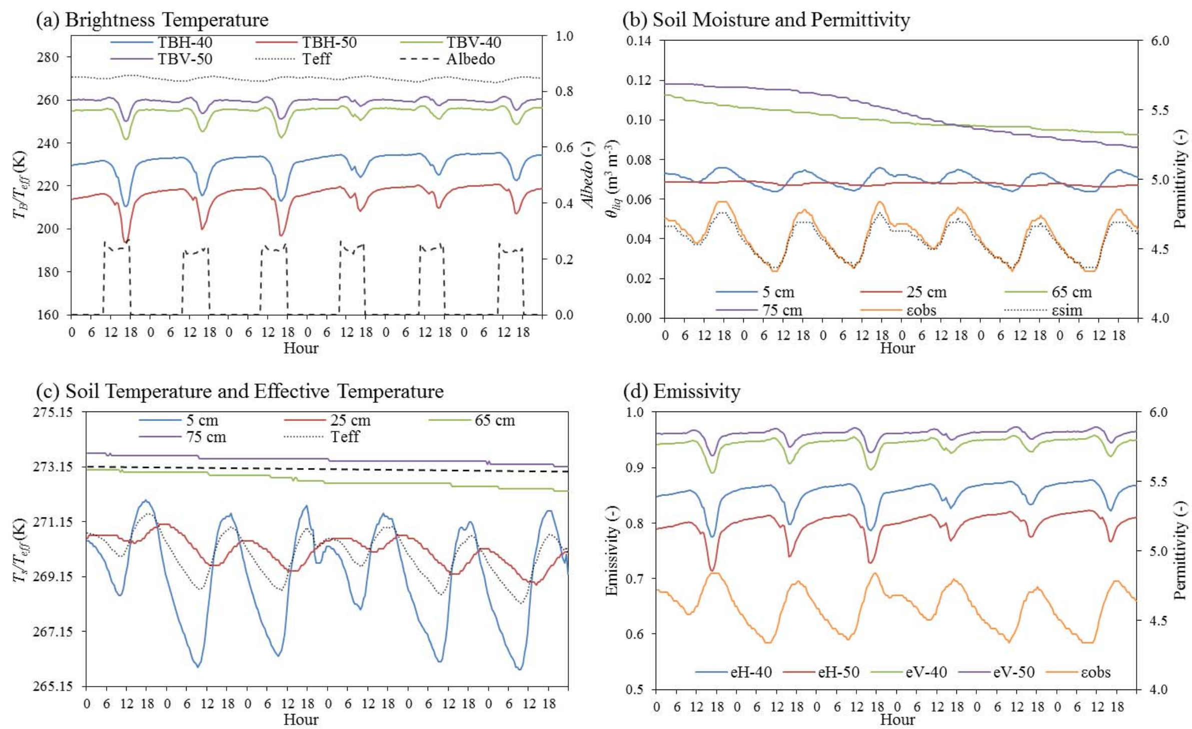

Fig. 5. Diurnal variations of (a) brightness temperature at horizontal ($T_{\mathrm{B}}^{\mathrm{H}}$) and vertical ($T_{\mathrm{B}}^{\mathrm{V}}$) polarizations for incidence angles of 40° and 50°, effective temperature (T_{eff}), and albedo, (b) liquid soil water (θ_{liq}) at different depths and permittivities (ε), (c) soil temperature (T_s) at different depths and effective temperatures (T_{eff}), and (d) emissivity at horizontal (e^{H}) and vertical (e^{V}) polarizations for incidence angles of 40° and 50° and permittivity (ε) for the freezing period January 1–6 (DOYs 1–6).

between 0 and 8 h between DOYs 88 and 93 (thawing period, Fig. 6), and the subsequent thawing results in the drop down of e^p and T_{B}^p. It should be noted that the phase of the e^p and T_{B}^p diurnal cycles do not match well with that of measured θ_{liq} at 5 cm, which infer that the L-band soil moisture sensing depth may be shallower than the *in situ* measured θ_{liq} depth. Indeed, Wegmüller [32] showed that a wet layer is formed at the surface when soil is thawing. It is also interesting to observe that the presence of snowfall/snowpack (indicated by much higher albedo value) sharply increases both e^p and T_{B}^p during the thawing period, and the T_{B}^p at horizontal polarization ($T_{\mathrm{B}}^{\mathrm{H}}$) is more sensitive to the presence of snow [30], [64].

Fig. 7 shows the angular dependency of T_{B}^p at different measured times (i.e., 0, 4, 8, 12, 16, and 20 h) for DOYs 1 and 88, which correspond to the typical freezing and thawing period. The angular characteristics of both freezing and thawing periods clearly reveal the typical Fresnel behavior, for which the T_{B}^p at horizontal polarization ($T_{\mathrm{B}}^{\mathrm{H}}$) monotonically decreases with increasing incidence angle [Fig. 7(a) and (c)] and the ones at vertical polarization [$T_{\mathrm{B}}^{\mathrm{V}}$, Fig. 7(b) and (d)] show a "Brewster-like" maximum at around 55°–60° and 60°–65° for the freezing and thawing periods, respectively. The thawing of ice during the freezing period as noted in Fig. 5 sharply decreases the measured T_{B}^p in both polarizations at 16 h [Fig. 7(a) and (b)], while the freezing of water during the thawing period (Fig. 6) significantly increases the T_{B}^p at 4–8 h [Fig. 7(c) and (d)].

V. Simulation of Diurnal Soil Freeze–Thaw Process

A. Model Inputs

To compute the emissivity of the soil-vegetation system using the passive version of the Tor Vergata emission model (Section III-A), several vegetation and soil parameters are required, such as LAI, leaf dimensions (e.g., thick-

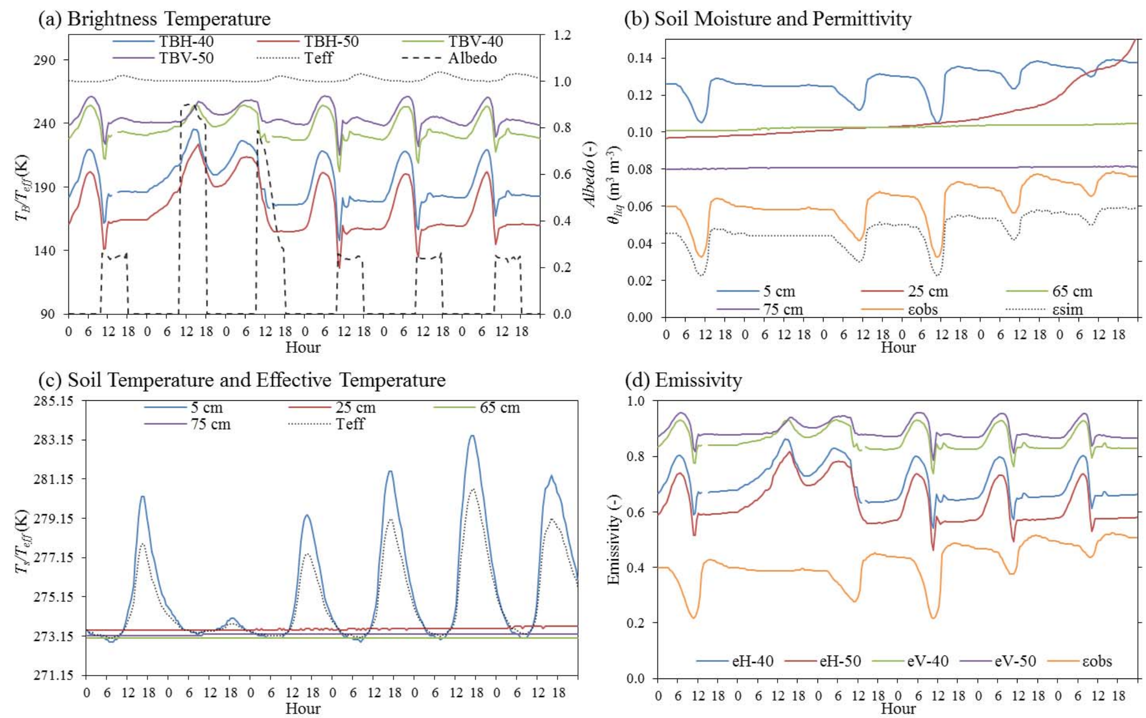

Fig. 6. Same as Fig. 5 but for the thawing period March 28 to April 2 (DOYs 88–93).

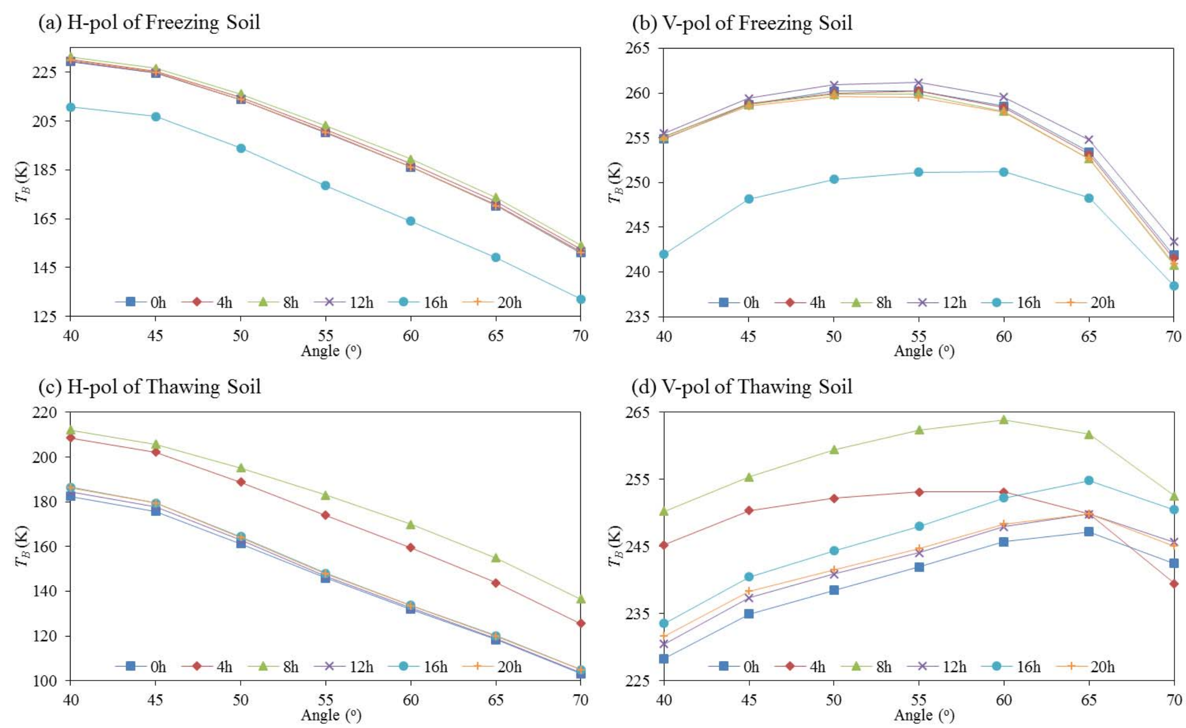

Fig. 7. Angular dependency of T_B at different measured times (i.e., 0, 4, 8, 12, 16, and 20 h) at (a) horizontal polarization (H-pol) and (b) vertical polarization (V-pol) for freezing period (DOY 1), and (c) H- and (d) V-pol for thawing period (DOY 88).

ness and radius), gravimetric water content, biomass and gravimetric water content of litter, ground surface roughness (i.e., height standard deviation and autocorrelation length), and soil permittivity. The leaf, litter, and surface roughness parameters have been derived from [38], where they were specifically calibrated for the Maqu site, and the LAI has been obtained from the MODIS product (Section II-C). Soil permittivity has been simulated using the four-phase dielectric mixing model [see (5)] that needs the soil texture, bulk density, and SMST of the top soil layer as input. The soil properties were measured via laboratory analysis (Section II-C), and three experiments are performed to obtain the SMST within the top soil layer. First, the average SMST measurements at 5 cm depth (Section II-B) are adopted (EXP1). Second, the four

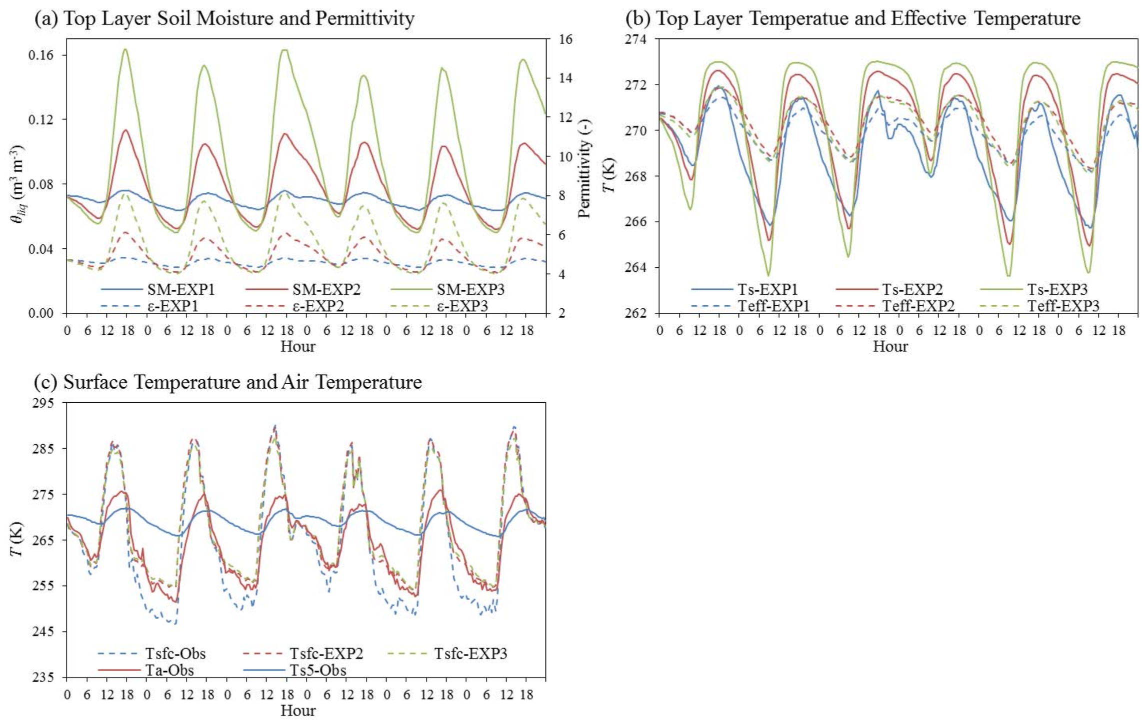

Fig. 8. Diurnal variations of (a) surface layer liquid soil water (θ_{liq}) and permittivity (ε), (b) soil temperature (T_s) and effective temperature (T_{eff}), and (c) surface temperature (T_{sfc}) and air temperature (T_a) produced by three numerical data sets for freezing period January 1–6 (DOYs 1–6).

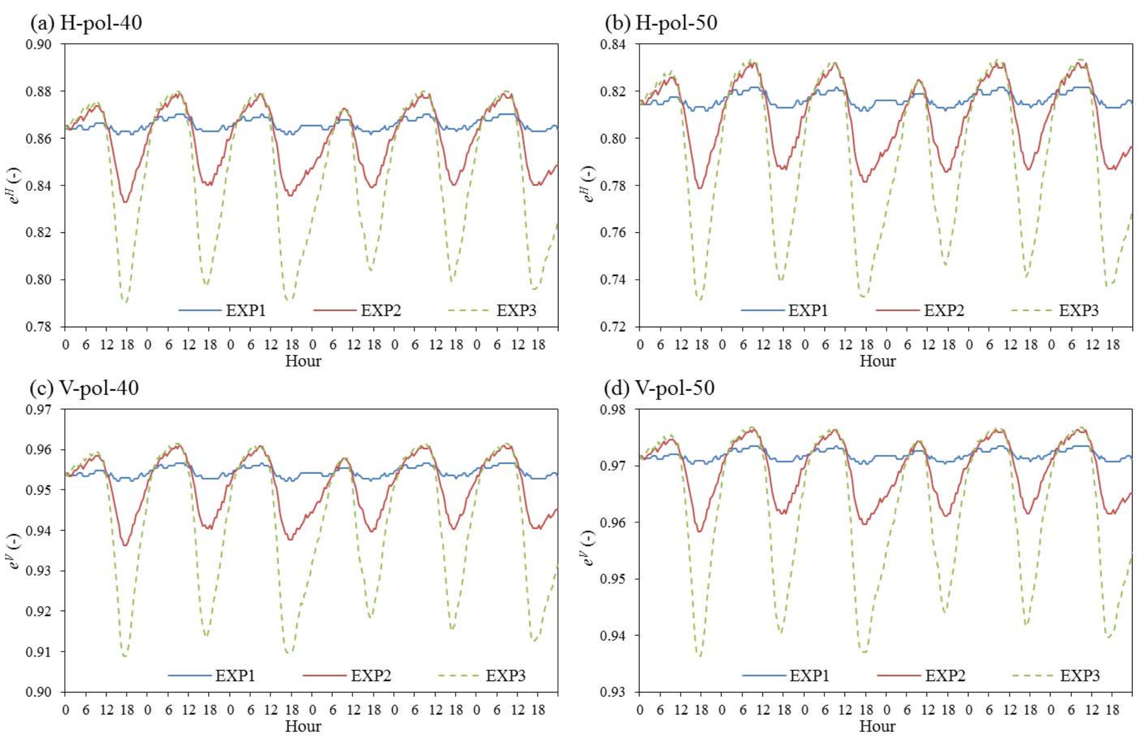

Fig. 9. Diurnal variations of emissivity at (a) horizontal polarization (H-pol, e^{H}) and (c) vertical polarization (V-pol, e^{V}) at an incidence angle of 40°, and (b) H- and (d) V-pol at an incidence angle of 50° produced by three numerical data sets for freezing period January 1–6 (DOYs 1–6).

standard layer (i.e., 0.1, 0.4, 1.0, and 2.0 m) configuration of the Noah LSM (Section III-D) is run to obtain the top layer SMST with midpoint at 5 cm (EXP2). Third, a five-layer (i.e., 0.05, 0.1, 0.4, 1.0, and 2.0 m) configuration of the Noah LSM is setup to obtain the top layer SMST with midpoint at shallower depth, i.e., 2.5 cm (EXP3).

The needed atmospheric forcing to drive the Noah LSM is obtained from the micrometeorological observing system

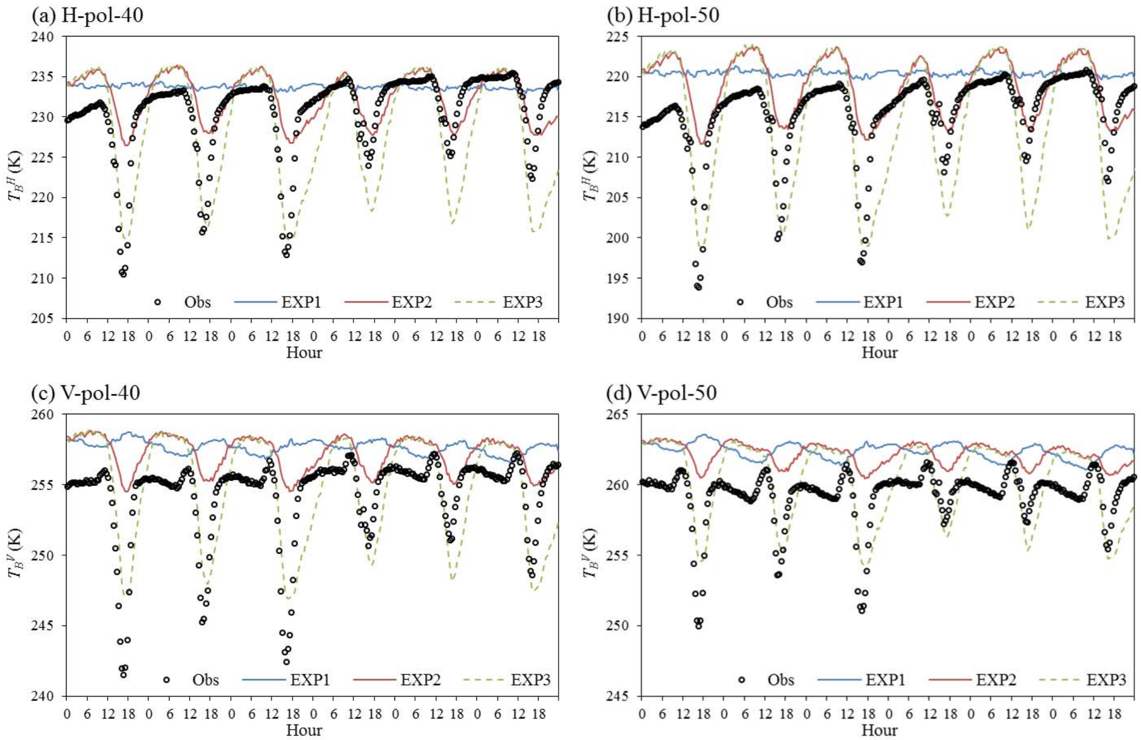

Fig. 10. Diurnal variations of measured and simulated brightness temperature at (a) horizontal polarization (H-pol, T_B^H) and (c) vertical polarization (V-pol, T_B^V) at an incidence angle of 40°, and (b) H- and (d) V-pol at an incidence angle of 50° produced by three numerical data sets for freezing period January 1–6 (DOYs 1–6).

(Section II-B), such as air temperature, relative humidity, wind speed, air pressure, upward and downward shortwave radiations, and downward longwave radiation. The soil hydraulic parameters are measured directly (Section II-C), and vegetation parameters (e.g., the number of root layers) are obtained from Noah's default land-cover database. Since the snowfall/snowpack measurements are not available, only the selected snow-free freezing period (DOYs 1–6, Section IV-B) is investigated. The thawing period (e.g., DOYs 88–93, Section IV-B) is not included in the present investigation due to the fact that a time delay is found between the phase of T_B^p diurnal cycle and measured θ_{liq} dynamics at 5 cm (Fig. 6) during this period, because the measured T_B^p signatures may be affected by: 1) the melting/refreezing of liquid water within the snowpack and/or 2) the freezing/thawing of infiltrated snow-melted water in the surface soil layer above 5 cm. In order to investigate the behavior of observed L-band signatures of soil diurnal freeze–thaw through comparison with the ELBARA-III measurements, the emissivity simulated with the Tor Vergata model is multiplied by the T_{eff} to obtain the T_B^p due to the fact that the LAI is very low (0.2, Table III), and thus the vegetation emission is low, particularly at L-band. Correspondingly, T_{eff} is estimated by (3) using the SMST profiles derived from either the *in situ* measurements (EXP1), or Noah simulations configured with four (EXP2) or five (EXP3) soil layers.

B. Model Simulation Results

Fig. 8(a) and (b) shows time series with a 30-min interval of the measured and simulated SMST at the top layer produced with the Noah LSM for the freezing period (DOYs 1–6), and the derived permittivity [Fig. 8(a)] using the four-phase dielectric mixing model and the T_{eff} [Fig. 8(b)] computed by (3) are shown as well. The air (T_a) and surface temperature (T_{sfc}) are further shown in Fig. 8(c). Fig. 8(c) shows that the amplitudes of T_a and T_{sfc} are much larger than the measured soil temperature at 5 cm, and the Noah simulations (EXP2 and EXP3) are able to capture the measured T_{sfc} dynamics while overestimate it during night and early morning (20–8 h). This overestimation can be related to the overestimation of thermal heat conductivity (κ_h) in the soil [65]. Since the *in situ* SMST measurements are collected at specific depths (e.g., 5 cm in the top layer), while the Noah simulations physically represent the layer averaged values (e.g., 0–10 cm for EXP2 and 0–5 cm for EXP3 in the top layer), which explains why the amplitudes of top layer soil temperature produced by the Noah LSM are larger than the measurements at 5 cm [Fig. 8(b)] due to the increasing amplitude of temperature closer to the surface. As such, the dynamic ranges of simulated θ_{liq} and permittivity [Fig. 8(a)] are larger than those of measurements, especially during the day when the ice is thawing because of the strongly coupled water and heat exchanges in the frozen soil [see (7) and (8)]. The mismatching of represented depth between measurements and simulations leads to these aforementioned SMST differences as also reported in [66]. It can also be found that: 1) the amplitudes of T_{eff} are smaller than those of top layer soil temperature [Fig. 8(b)] and 2) the differences between the T_{eff} produced with the three experiments are comparably small.

Figs. 9 and 10 show, respectively, the simulated emissivity and T_B^p values produced with the three data sets, and the ELBARA-III T_B^p measurements are also shown in Fig. 10

TABLE IV

COEFFICIENT OF DETERMINATION (R^2) AND RMSE COMPUTED BETWEEN THE MEASURED AND SIMULATED BRIGHTNESS TEMPERATURE AT HORIZONTAL (H-POL) AND VERTICAL (V-POL) POLARIZATION FOR INCIDENCE ANGLE OF 40° AND 50° PRODUCED BY THREE NUMERICAL DATA SETS FOR FREEZING PERIOD JANUARY 1–6 (DOYS 1–6)

Experiments	H-pol-40		H-pol-50		V-pol-40		V-pol-50	
	R^2	RMSE (K)	R^2	RMSE (K)	R^2	RMSE (K)	R^2	RMSE (K)
EXP1	0.005	5.98	0.104	6.98	0.141	4.70	0.113	3.86
EXP2	0.442	4.26	0.468	4.97	0.427	3.79	0.359	3.35
EXP3	0.479	5.56	0.495	6.04	0.469	2.84	0.405	2.34

for reference. Similar to the findings given in the previous section, it can be inferred that the permittivity effect (i.e., e^p) outweighs the temperature effect (i.e., T_{eff}) in controlling the T_B^p signatures of diurnal soil freeze–thaw (comparing Figs. 9 and 10). The T_B^p simulations produced by the EXP1 with the measured SMST as input do not indicate any obvious diurnal cycles at horizontal polarization [Fig. 10(a) and (b)], and the changes are opposite at vertical polarization [Fig. 10(c) and (d)] in comparison with the ELBARA-III measurements. These deficiencies are largely resolved by the EXP2 and EXP3 using the Noah simulated SMST that produce larger amplitudes of permittivity [Fig. 8(a)]. The error statistics, i.e., coefficient of determination (R^2) and RMSE, computed between the measured and simulated T_B^p are listed in Table IV, which further confirm the superiority of numerical experiments using the Noah simulations. Overall, the amplitudes of the simulated T_B^p produced by the EXP3 capture best those of measurements for both polarizations and angles, which indicates that the T_B^p signatures of diurnal soil freeze–thaw cycle is more sensitive to the liquid water content of the soil surface layer than the measurements taken at 5 cm depth. Similar findings have also been reported for the thawed soil [67], [68].

In general, the T_B^p signatures measured during soil thawing (e.g., starting of thawing and magnitude of thawed) are well captured by the EXP3, while the soil freezing process is poorly simulated. In comparison with the ELBARA-III measurements, the EXP3 simulations indicate a time delay of soil freezing and an overestimation of frozen amplitude. This can be explained by the fact that the Noah simulations represent the top soil as a homogeneous single layer, while in reality, the top soil may form a heterogeneous structure, e.g., made up of frozen and unfrozen soil. The overestimation of T_{sfc} by the Noah simulations noted during night and morning [Fig. 8(c)] may further contribute to the time delay of top layer soil freezing and overestimation of T_B^p. In addition, conspicuous peaks noted in the measured T_B^p signatures before the soil thawing are not reproduced by the EXP3 simulations, which may be related to the sun reflection as reported in [69]. It can also be found that the measured T_B^p signatures show some day-to-day variations of minimum values that are not well captured by the EXP3 simulations, indicating that additional work is needed to further refine the integrated Tor Vergata model and Noah LSM developed in this study.

VI. CONCLUSION

We investigate the L-band emission characteristics during soil freeze–thaw cycle via combined analysis of tower-based brightness temperature (T_B^p, with p = H, V) measurements with ELBARA-III instrument and simulations performed with a model of soil emission considering vertical variations of permittivity and soil temperature. The soil emission is estimated by the IEM model with the soil permittivity computed by the four-phase dielectric mixing model, and vegetation effects are modeled using the Tor Vergata discrete emission model. The T_B^p is then derived from the computed emissivity (e^p) via multiplication with the soil effective temperature (T_{eff}) for comparison with those ELBARA-III T_B^p measurements.

The ELBARA-III radiometer is set up within a well-instrumented regional SMST monitoring network that is located in the SRYR over the northeastern part of the Tibetan Plateau. The ELBARA-III measurements T_B^p are composed of elevation scanning sequences (40°–70° relative to nadir in steps of 5°) toward the ground performed every 30 min and zenith (sky) measurements performed once per day. The T_B^p measurements are further supported by continuous measurements of micrometeorological variables and SMST as well as soil and vegetation parameter measurements.

Distinct periods of freezing (frozen) and thawing (thawed) are detected from the long-term comprehensive measurements collected between January 1 (DOY 1) and April 5 (DOY 96), 2016, and further analyses show that: 1) the T_B^p measurements generally remain stable during the freezing period before DOY 77, and then drop down and exhibit comparably large variations due to the onset of soil thawing; 2) the emission depth ranges between 10 and 30 cm with the shallowest one located above 10 cm when the soil is thawed; 3) the T_{eff} is comparable with the temperature at 25 cm depth when the soil liquid water is frozen, while it is closer to the one at 5 cm when the soil ice is thawing; and 4) the PR is a suitable indicator to detect the soil freezing or thawing.

Two short continuous observation periods (DOYs 1–6 and DOYs 88–93) are selected to further investigate the diurnal characteristics of freezing and thawing soil, and it demonstrates that: 1) the four-phase dielectric mixing model well simulates the measurement of permittivity when the soil is frozen, although underestimates it when the soil is thawed; 2) the T_{eff} variations are much smaller than those of T_B^p; 3) obvious diurnal variations are found for the emissivity, indicating that the changing permittivity associated with the diurnal freeze–thaw transition in the top soil layer dominates the diurnal variation of T_B^p; and 4) the angular characteristics clearly reveal the typical Fresnel behavior.

Moreover, the Tor Vergata simulations configured with the SMST derived from either *in situ* measurements or Noah simulations indicate that the T_B^p signatures of diurnal soil freeze–thaw cycle are more sensitive to the liquid water content of the soil surface layer than the measurements taken at 5 cm depth. As such, the current SMST monitoring networks operated on the Tibetan Plateau [11], [12] are recommended to measure top layer soil moisture closer to the surface for capturing the L-band signatures of diurnal soil freeze–thaw. However, scientists should carefully consider the penetration depth of the sensors itself; otherwise, the sensor readings will be affected by air, particularly under dry soil conditions. Alternatively, the mechanistic model such as the Noah LSM adopted in this study can be potentially used to produce SMST over a shallower layer. Additional work is still needed to refine the integrated Tor Vergata model and Noah LSM developed in this study, which can be then utilized to interpret the SMOS/SMAP T_B^p signatures of soil F/T state.

Acknowledgment

The authors would like to thank the European Space Agency (ESA) for providing ELBARA-III instrument. They would also like to thank two anonymous reviewers for their constructive comments.

References

[1] T. Zhang, R. G. Barry, K. Knowles, J. A. Heginbottom, and J. Brown, "Statistics and characteristics of permafrost and ground-ice distribution in the Northern Hemisphere," *Polar Geograph.*, vol. 23, no. 2, pp. 132–154, Apr. 1999.

[2] D. Guo and H. Wang, "Simulation of permafrost and seasonally frozen ground conditions on the Tibetan Plateau, 1981–2010," *J. Geophys. Res., Atmos.*, vol. 118, no. 11, pp. 5216–5230, 2013.

[3] O. T. Farouki, *Thermal Properties of Soils*, vol. 11. Clausthal-Zellerfeld, Gemany: Trans. Tech. Publ., 1986.

[4] Y. Zhang, S. K. Carey, and W. L. Quinton, "Evaluation of the algorithms and parameterizations for ground thawing and freezing simulation in permafrost regions," *J. Geophys. Res., Atmos.*, vol. 113, no. D17, p. D17116, 2008.

[5] L. Zhao, D. M. Gray, and D. H. Male, "Numerical analysis of simultaneous heat and mass transfer during infiltration into frozen ground," *J. Hydrol.*, vol. 200, pp. 345–363, Dec. 1997.

[6] E. Poutou, G. Krinner, C. Genthon, and N. de Noblet-Ducoudré, "Role of soil freezing in future boreal climate change," *Climate Dyn.*, vol. 23, no. 6, pp. 621–639, 2004.

[7] P. Viterbo, A. Beljaars, J.-F. Mahfouf, and J. Teixeira, "The representation of soil moisture freezing and its impact on the stable boundary layer," *Quart. J. Roy. Meteorol. Soc.*, vol. 125, no. 559, pp. 2401–2426, 1999.

[8] D. M. Lawrence and A. G. Slater, "Incorporating organic soil into a global climate model," *Climate Dyn.*, vol. 30, no. 2, pp. 145–160, 2008.

[9] G. Cheng and T. Wu, "Responses of permafrost to climate change and their environmental significance, Qinghai-Tibet Plateau," *J. Geophys. Res., Earth Surf.*, vol. 112, p. F02S03, Jun. 2007.

[10] Q. Wu and T. Zhang, "Changes in active layer thickness over the Qinghai-Tibetan Plateau from 1995 to 2007," *J. Geophys. Res., Atmos.*, vol. 115, p. D09107, May 2010.

[11] Z. Su *et al.*, "The Tibetan Plateau observatory of plateau scale soil moisture and soil temperature (Tibet-Obs) for quantifying uncertainties in coarse resolution satellite and model products," *Hydrol. Earth Syst. Sci.*, vol. 15, no. 7, pp. 2303–2316, 2011.

[12] K. Yang *et al.*, "A multiscale soil moisture and freeze–thaw monitoring network on the third pole," *Bull. Amer. Meteorol. Soc.*, vol. 94, pp. 1907–1916, Dec. 2013.

[13] Z. Su, P. de Rosnay, J. Wen, L. Wang, and Y. Zeng, "Evaluation of ECMWF's soil moisture analyses using observations on the Tibetan Plateau," *J. Geophys. Res., Atmos.*, vol. 118, no. 11, pp. 5304–5318, 2013.

[14] Y. Chen, K. Yang, J. Qin, L. Zhao, W. Tang, and M. Han, "Evaluation of AMSR-E retrievals and GLDAS simulations against observations of a soil moisture network on the central Tibetan Plateau," *J. Geophys. Res. Atmos.*, vol. 118, no. 10, pp. 4466–4475, 2013.

[15] Y. Zeng *et al.*, "Blending satellite observed, model simulated, and *in situ* measured soil moisture over tibetan plateau," *Remote Sens.*, vol. 8, no. 3, p. 268, 2016.

[16] L. Cuo *et al.*, "Frozen soil degradation and its effects on surface hydrology in the northern Tibetan Plateau," *J. Geophys. Res., Atmos.*, vol. 120, pp. 8276–8298, Aug. 2015.

[17] D. Zheng *et al.*, "Impacts of Noah model physics on catchment-scale runoff simulations," *J. Geophys. Res., Atmos.*, vol. 121, pp. 807–832, Jan. 2016.

[18] D. Zheng, R. Van Der Velde, Z. Su, J. Wen, and X. Wang, "Assessment of Noah land surface model with various runoff parameterizations over a Tibetan river," *J. Geophys. Res. Atmos.*, vol. 122, pp. 1488–1504, Feb. 2017.

[19] J. S. Kimball, K. C. McDonald, S. W. Running, and S. E. Frolking, "Satellite radar remote sensing of seasonal growing seasons for boreal and subalpine evergreen forests," *Remote Sens. Environ.*, vol. 90, no. 2, pp. 243–258, 2004.

[20] V. Naeimi *et al.*, "ASCAT surface state flag (SSF): Extracting information on surface freeze/thaw conditions from backscatter data using an empirical threshold-analysis algorithm," *IEEE Trans. Geosci. Remote Sens.*, vol. 50, no. 7, pp. 2566–2582, Jul. 2012.

[21] S. Frolking, K. C. McDonald, J. S. Kimball, J. B. Way, R. Zimmermann, and S. W. Running, "Using the space-borne NASA scatterometer (NSCAT) to determine the frozen and thawed seasons," *J. Geophys. Res., Atmos.*, vol. 104, no. D22, pp. 27895–27907, 1999.

[22] Y. Kim, J. S. Kimball, K. Zhang, and K. C. McDonald, "Satellite detection of increasing Northern Hemisphere non-frozen seasons from 1979 to 2008: Implications for regional vegetation growth," *Remote Sens. Environ.*, vol. 121, pp. 472–487, Jun. 2012.

[23] T. Zhao, L. Zhang, L. Jiang, S. Zhao, L. Chai, and R. Jin, "A new soil freeze/thaw discriminant algorithm using AMSR-E passive microwave imagery," *Hydrol. Process.*, vol. 25, no. 11, pp. 1704–1716, 2011.

[24] T. Zhang and R. L. Armstrong, "Soil freeze/thaw cycles over snow-free land detected by passive microwave remote sensing," *Geophys. Res. Lett.*, vol. 28, no. 5, pp. 763–766, 2001.

[25] Y. H. Kerr, P. Waldteufel, J. P. Wigneron, J. Martinuzzi, J. Font, and M. Berger, "Soil moisture retrieval from space: The Soil Moisture and Ocean Salinity (SMOS) mission," *IEEE Trans. Geosci. Remote Sens.*, vol. 39, no. 8, pp. 1729–1735, Aug. 2001.

[26] K. Rautiainen *et al.*, "Detection of soil freezing from L-band passive microwave observations," *Remote Sens. Environ.*, vol. 147, pp. 206–218, May 2014.

[27] K. Rautiainen *et al.*, "SMOS prototype algorithm for detecting autumn soil freezing," *Remote Sens. Environ.*, vol. 180, pp. 346–360, Jul. 2016.

[28] A. Roy *et al.*, "Evaluation of spaceborne L-band radiometer measurements for terrestrial freeze/thaw retrievals in Canada," *IEEE J. Sel. Topics Appl. Earth Observ. Remote Sens.*, vol. 8, no. 9, pp. 4442–4459, Sep. 2015.

[29] D. Entekhabi *et al.*, "The Soil Moisture Active Passive (SMAP) mission," *Proc. IEEE*, vol. 98, no. 5, pp. 704–716, May 2010.

[30] M. Schwank *et al.*, "Snow density and ground permittivity retrieved from L-band radiometry: A synthetic analysis," *IEEE J. Sel. Topics Appl. Earth Observ. Remote Sens.*, vol. 8, no. 8, pp. 3833–3845, Aug. 2015.

[31] M. Schwank *et al.*, "Model for microwave emission of a snow-covered ground with focus on L band," *Remote Sens. Environ.*, vol. 154, pp. 180–191, Nov. 2014.

[32] U. Wegmüler, "The effect of freezing and thawing on the microwave signatures of bare soil," *Remote Sens. Environ.*, vol. 33, pp. 123–135, Aug. 1990.

[33] L. Zhang, T. Zhao, L. Jiang, and S. Zhao, "Estimate of phase transition water content in freeze–thaw process using microwave radiometer," *IEEE Trans. Geosci. Remote Sens.*, vol. 48, no. 12, pp. 4248–4255, Dec. 2010.

[34] M. Schwank, M. Stahli, H. Wydler, J. Leuenberger, C. Matzler, and H. Fluhler, "Microwave L-band emission of freezing soil," *IEEE Trans. Geosci. Remote Sens.*, vol. 42, no. 6, pp. 1252–1261, Jun. 2004.

[35] K. Rautiainen *et al.*, "L-band radiometer observations of soil processes in boreal and subarctic environments," *IEEE Trans. Geosci. Remote Sens.*, vol. 50, no. 5, pp. 1483–1497, May 2012.

[36] M. Schwank *et al.*, "ELBARA II, an L-band radiometer system for soil moisture research," *Sensors*, vol. 10, no. 1, pp. 584–612, 2010.

[37] M. Bracaglia, P. Ferrazzoli, and L. Guerriero, "A fully polarimetric multiple scattering model for crops," *Remote Sens. Environ.*, vol. 54, pp. 170–179, Dec. 1995.

[38] L. Dente, P. Ferrazzoli, Z. Su, R. van der Velde, and L. Guerriero, "Combined use of active and passive microwave satellite data to constrain a discrete scattering model," *Remote Sens. Environ.*, vol. 155, pp. 222–238, Dec. 2014.

[39] L. Dente, Z. Vekerdy, J. Wen, and Z. Su, "Maqu network for validation of satellite-derived soil moisture products," *Int. J. Appl. Earth Observ. Geoinf.*, vol. 17, pp. 55–65, Jul. 2012.

[40] D. Zheng *et al.*, "Augmentations to the Noah model physics for application to the yellow river source area. Part I: Soil water flow," *J. Hydrometeorol.*, vol. 16, no. 6, pp. 2659–2676, 2015.

[41] M. Schwank, C. Matzler, M. Guglielmetti, and H. Fluhler, "L-band radiometer measurements of soil water under growing clover grass," *IEEE Trans. Geosci. Remote Sens.*, vol. 43, no. 10, pp. 2225–2237, Oct. 2005.

[42] G. C. Topp, J. L. Davis, and A. P. Annan, "Electromagnetic determination of soil water content: Measurements in coaxial transmission lines," *Water Resour. Res.*, vol. 16, no. 3, pp. 574–582, Jun. 1980.

[43] D. Zheng, R. van der Velde, Z. Su, M. J. Booij, A. Y. Hoekstra, and J. Wen, "Assessment of roughness length schemes implemented within the Noah land surface model for high-altitude regions," *J. Hydrometeorol.*, vol. 15, no. 3, pp. 921–937, 2014.

[44] D. Zheng *et al.*, "Under-canopy turbulence and root water uptake of a Tibetan meadow ecosystem modeled by Noah-MP," *Water Resour. Res.*, vol. 51, no. 7, pp. 5735–5755, 2015.

[45] R. Myneni, Y. Knyazikhin, and T. Park, "MCD15A3H MODIS/terra+aqua leaf area index/FPAR 4-day L4 global 500m SIN grid V006," NASA EOSDIS Land Processes DAAC, Tech. Rep., 2015.

[46] P. Ferrazzoli and L. Guerriero, "Passive microwave remote sensing of forests: A model investigation," *IEEE Trans. Geosci. Remote Sens.*, vol. 34, no. 2, pp. 433–443, Mar. 1996.

[47] P. Ferrazzoli and L. Guerriero, "Radar sensitivity to tree geometry and woody volume: A model analysis," *IEEE Trans. Geosci. Remote Sens.*, vol. 33, no. 2, pp. 360–371, Mar. 1995.

[48] H. J. Eom and A. K. Fung, "A scatter model for vegetation up to Ku-band," *Remote Sens. Environ.*, vol. 15, no. 3, pp. 185–200, 1984.

[49] F. T. Ulaby *et al.*, *Microwave Radar and Radiometric Remote Sensing*. Norwood, MA, USA: Artech House, 2014.

[50] A. K. Fung, *Microwave Scattering and Emission Models and Their Applications*. Norwood, MA, USA: Artech House, 1994.

[51] P. Ferrazzoli, J. P. Wigneron, L. Guerriero, and A. Chanzy, "Multifrequency emission of wheat: Modeling and applications," *IEEE Trans. Geosci. Remote Sens.*, vol. 38, no. 6, pp. 2598–2607, Nov. 2000.

[52] A. D. Vecchia *et al.*, "Modeling the multifrequency emission of broadleaf forests and their components," *IEEE Trans. Geosci. Remote Sens.*, vol. 48, no. 1, pp. 260–272, Jan. 2010.

[53] T. Pellarin *et al.*, "Two-year global simulation of L-band brightness temperatures over land," *IEEE Trans. Geosci. Remote Sens.*, vol. 41, no. 9, pp. 2135–2139, Sep. 2003.

[54] B. J. Choudhury, T. J. Schmugge, and T. Mo, "A parameterization of effective soil temperature for microwave emission," *J. Geophys. Res., Oceans*, vol. 87, no. C2, pp. 1301–1304, 1982.

[55] S. Lv, J. Wen, Y. Zeng, H. Tian, and Z. Su, "An improved two-layer algorithm for estimating effective soil temperature in microwave radiometry using *in situ* temperature and soil moisture measurements," *Remote Sens. Environ.*, vol. 152, pp. 356–363, Sep. 2014.

[56] J. P. Wigneron, L. Laguerre, and Y. H. Kerr, "A simple parameterization of the L-band microwave emission from rough agricultural soils," *IEEE Trans. Geosci. Remote Sens.*, vol. 39, no. 8, pp. 1697–1707, Aug. 2001.

[57] J. R. Birchak, C. G. Gardner, J. E. Hipp, and J. M. Victor, "High dielectric constant microwave probes for sensing soil moisture," *Proc. IEEE*, vol. 62, no. 1, pp. 93–98, Jan. 1974.

[58] M. Stähli and D. Stadler, "Measurement of water and solute dynamics in freezing soil columns with time domain reflectometry," *J. Hydrol.*, vol. 195, pp. 352–369, Aug. 1997.

[59] M. C. Dobson, F. T. Ulaby, M. T. Hallikainen, and M. A. El-Rayes, "Microwave dielectric behavior of wet soil-Part II: Dielectric mixing models," *IEEE Trans. Geosci. Remote Sens*, vol. 23, no. 1, pp. 35–46, Jan. 1985.

[60] D. Zheng *et al.*, "Augmentations to the Noah model physics for application to the Yellow River source area. Part II: Turbulent heat fluxes and soil heat transport," *J. Hydrometeorol.*, vol. 16, no. 6, pp. 2677–2694, 2015.

[61] V. Koren, J. Schaake, K. Mitchell, Q.-Y. Duan, F. Chen, and J. M. Baker, "A parameterization of snowpack and frozen ground intended for NCEP weather and climate models," *J. Geophys. Res., Atmos.*, vol. 104, no. D16, pp. 19569–19585, 1999.

[62] M. J. Malik, R. van der Velde, Z. Vekerdy, Z. Su, and M. F. Salman, "Semi-empirical approach for estimating broadband albedo of snow," *Remote Sens. Environ.*, vol. 115, pp. 2086–2095, Aug. 2011.

[63] G. N. Flerchinger, M. S. Seyfried, and S. P. Hardegree, "Using soil freezing characteristics to model multi-season soil water dynamics," *Vadose Zone J.*, vol. 5, no. 4, pp. 1143–1153, 2006.

[64] J. Lemmetyinen *et al.*, "Snow density and ground permittivity retrieved from L-band radiometry: Application to experimental data," *Remote Sens. Environ.*, vol. 180, pp. 377–391, Jul. 2016.

[65] H. Bao, T. Koike, K. Yang, L. Wang, M. Shrestha, and P. Lawford, "Development of an enthalpy-based frozen soil model and its validation in a cold region in China," *J. Geophys. Res., Atmos.*, vol. 121, no. 10, pp. 5259–5280, 2016.

[66] Y. Xia *et al.*, "Validation of Noah-simulated soil temperature in the North American land data assimilation system phase 2," *J. Appl. Meteorol. Climatol.*, vol. 52, no. 2, pp. 455–471, Feb. 2012.

[67] M.-J. Escorihuela, A. Chanzy, J.-P. Wigneron, and Y. Kerr, "Effective soil moisture sampling depth of L-band radiometry: A case study," *Remote Sens. Environ.*, vol. 114, no. 5, pp. 995–1001, 2010.

[68] S. Raju, A. Chanzy, J.-P. Wigneron, J.-C. Calvet, Y. Kerr, and L. Laguerre, "Soil moisture and temperature profile effects on microwave emission at low frequencies," *Remote Sens. Environ.*, vol. 54, no. 2, pp. 85–97, 1995.

[69] K. Schneeberger, C. Stamm, C. Matzler, and H. Fluhler, "Ground-based dual-frequency radiometry of bare soil at high temporal resolution," *IEEE Trans. Geosci. Remote Sens.*, vol. 42, no. 3, pp. 588–595, Mar. 2004.

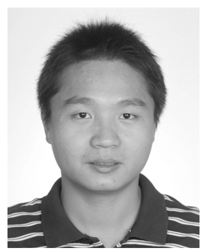

Donghai Zheng received the M.A. degree in remote sensing from Beijing Normal University, Beijing, China, in 2010, and the Ph.D. degree in hydrometeorology from the University of Twente, Enschede, The Netherlands, in 2015.

He is currently a Post-Doctoral Researcher with the Water Resources Department, Faculty of Geo-Information Science and Earth Observation, University of Twente, where he is involved in an NWO-GO project "Modelling Freeze-Thaw Processes with Active and Passive Microwave Observations." His research interests include land surface modeling, soil moisture retrieval using both active and passive microwave measurements, and laboratory and *in situ* measurements of soil moisture.

Xin Wang received the B.A. degree in atmospheric science from Nanjing University, Nanjing, China, in 2007, and the Ph.D. degree in meteorology from the University of Chinese Academy of Sciences, Beijing, China, in 2012.

He is currently an Assistant Professor with the Northwest Institute of Eco-Environment and Resources, Chinese Academy of Sciences, Lanzhou, China. His research interests include the soil moisture and freeze/thaw cycle observation and retrieval using passive microwave measurements in Tibet and remote sensing land hydrological cycle in Yellow River source catchment with passive microwave both on ground-based and spaceborne radiometer measurements.

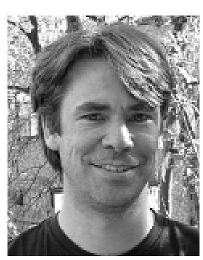

Rogier van der Velde received the M.Sc. degree in hydrology from Wageningen University, Wageningen, The Netherlands, in 2004, and the Ph.D. degree in satellite hydrology from the University of Twente, Enschede, The Netherlands, in 2010.

He is currently an Assistant Professor with the Water Resources Department, Faculty of Geo-Information Science and Earth Observation, University of Twente. His research interests include soil moisture monitoring using both active and passive microwave remote sensing techniques and its validation and application for water resources and agricultural management.

Yijian Zeng received the Ph.D. degree from the University of Twente, Enschede, The Netherlands, in 2012.

He is currently an Assistant Professor with the Water Resources Department, Faculty of Geo-Information Science and Earth Observation, University of Twente. His research interests include land-atmosphere interaction via hydrologic processes and how the interaction affects the climate system, generation of consistent climate data record using multisources of geo-datasets, physical mechanisms of land surface models, and the application of data assimilation.

Jun Wen received the B.A. degree in meteorology from Peking University, Beijing, China, in 1988, the M.A. degree in meteorology from Lanzhou University, Lanzhou, China, in 1995, and the Ph.D. degree in meteorology from the Chinese Academy of Sciences, Lanzhou, in 1999.

He is currently a Professor with the College of Atmospheric Sciences, Chengdu University of Information Technology, Chengdu, China. His research interests include remote sensing and data assimilation, land surface modeling, and climate change.

Zuoliang Wang received the B.A. degree from Northwest Normal University, Lanzhou, China, in 2014.

He is currently an Assistant Engineer with the Northwest Institute of Eco-Environment and Resources, Chinese Academy of Sciences, Lanzhou. His research interests include the observation and simulation of soil freeze-thaw process.

Mike Schwank was born in Zürich, Switzerland, in 1966. He received the bachelor's degree in electrical engineering and the Ph.D. degree in physics from ETH Zürich, Zürich, in 1989 and 1999, respectively.

He was with GAMMA, Gümligen, Switzerland, from 2007 to 2009 and since 2013 and also with the Swiss Federal Research Institute WSL, Birmensdorf, Switzerland, on a part-time basis. He has experience in industrial research and development in the fields of microoptics and telecommunications from 1999 to 2003. He guides Ph.D. students and coordinates large research projects such as Terrestrial Environmental Observatories. His research interests include microwave remote sensing studies in support of Soil Moisture and Ocean Salinity and future satellite missions.

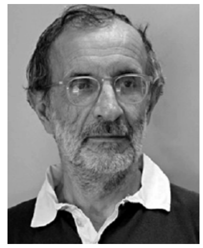

Paolo Ferrazzoli (M'94–SM'06) received the bachelor's degree from the Sapienza University of Rome, Rome, Italy, in 1972.

In 1974, he joined Telespazio Spa, Italy, where he focused on antennas, slantpath propagation, and advanced satellite telecommunication systems. In 1984, he joined Tor Vergata University of Rome, Rome, where he is currently teaching microwaves, radiowave propagation, and electromagnetic fields. His research interests include microwave remote sensing of vegetated terrains, with a particular emphasis on electromagnetic modeling.

Mr. Ferrazzoli was a member of the Technical Program Committee of IGARSS Conferences from 2012 to 2017. In the framework of ESA SMOS Project, he has been a member of the Science Advisory Group and the Quality Working Group. He has been involved in international experimental remote sensing campaigns such as AGRISAR, AGRISCATT, MAESTRO-1, MAC-Europe, and SIR-C/X-SAR. He has participated in the coordinating team of the European Radar-Optical Research Assemblage Project, funded by EEC, establishing an assemblage among several European researchers working in radar applications. He was the Chair of MICRORAD 2012 International Meeting.

Zhongbo (Bob) Su received the M.Sc. degree in hydrological engineering from Integrating the Healthcare Enterprise, Delft, The Netherlands, and the Ph.D. degree in civil engineering from Ruhr University, Bochum, Germany.

He is currently a Professor of Spatial Hydrology and Water Resources Management, Faculty of Geo-Information Science and Earth Observation, University of Twente, Enschede, The Netherlands, where he is the Chairman with the Department of Water Resources. His research interests include remote sensing and numerical modeling of land surface processes and interactions with the atmosphere, earth observation of water cycle and applications in climate, ecosystem and water resources studies, as well as monitoring food security, and water-related disasters.